

Evolution of Indian Ocean dipole and its forcing mechanisms in the absence of ENSO

Hui Wang^{1,3} · Raghu Murtugudde² · Arun Kumar¹

Received: 12 February 2015 / Accepted: 4 January 2016 / Published online: 12 January 2016
© Springer-Verlag Berlin Heidelberg 2016

Abstract The evolution of Indian Ocean dipole (IOD) and its forcing mechanisms are examined based on the analysis of coupled model simulations that allow or suppress the El Niño-Southern Oscillation (ENSO) mode of variability. The model can reproduce the most salient observed features of IOD even without ENSO, including the relationships between the eastern and western poles at both the surface and subsurface, as well as their seasonality. This suggests that ENSO is not fundamental for the existence of IOD. It is demonstrated that cold (warm) sea surface temperature (SST) anomalies in the eastern Indian Ocean associated with IOD can be initiated by springtime Indonesian rainfall deficit (surplus) through local surface wind response. The growth of the SST anomalies depends on the initial local subsurface condition. Both the air–sea interaction and surface–subsurface interaction contribute to the development of IOD. The evolution of IOD can be represented by two leading extended empirical orthogonal function (EEOF) modes of *tropical* surface–subsurface Indian Ocean temperatures; one stationary and the other non-stationary. The onset, growth, and termination of IOD, as well as the transition to an opposite phase, can be interpreted as alternations between the non-propagating mode (EEOF1) and the eastward-propagating Kelvin wave (EEOF2). The evolution of IOD is also accompanied by a

westward-propagating Rossby wave which is captured in the EEOF1 of the *subtropical* surface–subsurface Indian Ocean temperatures. Therefore, both Bjerknes feedback and a delayed oscillator operate during the evolution of IOD in the absence of ENSO also.

Keywords Indian Ocean dipole · El Niño-Southern Oscillation (ENSO) · Climate modeling

1 Introduction

The Indian Ocean dipole (IOD), also referred to as the Indian Ocean Zonal Mode, has received much attention since its discovery at the end of the twentieth century (e.g., Saji et al. 1999; Webster et al. 1999; Murtugudde et al. 2000). As an intrinsic mode of variability of tropical Indian Ocean, it has significant climate impacts across broad spatial and temporal scales. Despite the continued debate about whether this is indeed a dipole (Zhao and Nigam 2015) and a lack of mechanistic explanations for its phasing in boreal fall, IOD has been argued to be predictable (Luo et al. 2007) and also to influence various local and remote processes such as the North Indian Ocean tropical cyclones (Yuan and Cao 2013), the Indian summer monsoon (Gadgil et al. 2004; Pokhrel et al. 2012), the Madden-Julian Oscillation (Ajayamohan et al. 2009; Wilson et al. 2013), the evolution of El Niño-Southern Oscillation (ENSO; Wu and Kirtman 2004; Annamalai et al. 2005), and may help ENSO prediction at longer lead times (Izumo et al. 2010; Webster and Hoyos 2010).

The mechanisms responsible for the onset and evolution of IOD have been attributed to several physical processes: it can be triggered by ENSO forcing (Yu and Lau 2005; Wang and Wang 2014); induced by changes in the

✉ Hui Wang
hui.wang@noaa.gov

¹ NOAA/NWS/NCEP/Climate Prediction Center, 5830 University Research Court, NCWCP, College Park, MD 20740, USA

² ESSIC, University of Maryland, College Park, MD 20740, USA

³ Innovim, Greenbelt, MD 20770, USA

Pacific Walker circulation (Annamalai et al. 2003); initiated by severe cyclones over the Bay of Bengal (Francis et al. 2007); caused by western Arabian Sea anomalous upwelling (Izumo et al. 2008); or could originate from a subtropical IOD (Feng et al. 2014). Similar to the development of El Niño (Jin 1997) and Atlantic Niño (Keenlyside and Latif 2007; Lübbecke 2013), the growth and decay of IOD could also involve a positive atmosphere–ocean feedback (Annamalai et al. 2003; Wang and Wang 2014), the so-called Bjerknes feedback, as well as a negative ocean feedback (McPhaden and Nagura 2014), referred to as the delayed oscillator (Suarez and Schopf 1988; Battisti and Hirst 1989).

The delayed oscillator model, which was originally developed as the mechanism that provides negative feedback and limits the growing mode due to Bjerknes feedback during the evolution of an ENSO (Suarez and Schopf 1988), has also been considered as a viable mechanism in the tropical Atlantic (Lübbecke 2013) and Indian Oceans (Yamagata et al. 2004; Rao and Behera 2005). The processes involve eastward-propagating Kelvin waves reflected as Rossby waves at the eastern boundary and westward-propagating Rossby waves reflected as Kelvin waves at the western boundary.

The relationship between the dipole in sea surface temperature (SST) and the dipole in subsurface Indian Ocean, as well as the relationship between the eastern and western poles of IOD, is an important issue in understanding IOD variability (e.g., Sayantani and Gnanaseelan 2014). It is argued that the dipole of SST becomes a monopole after the removal of the ENSO-related signal, whereas the dipole structure still exists in the subsurface (Zhao and Nigam 2015). Ocean model simulations reveal that the surface and subsurface dipoles are highly correlated (Shinoda et al. 2004). It is also found that the surface dipole is well correlated with ENSO, but the subsurface dipole is not. Shinoda et al. (2004) also suggested two types of surface IOD, viz., the ENSO-forced surface dipole and the subsurface-induced surface dipole. The latter is controlled by the wind-driven oceanic Kelvin and Rossby waves (Rao et al. 2002) and is largely independent of ENSO. Clearly, the air–sea interaction and the surface–subsurface interaction, as well as the teleconnection to ENSO, all contribute to the variation of the surface dipole.

Whether IOD is primarily driven by ENSO or is independent of ENSO has also been a topic of heated debate. A weak correlation between IOD and the Niño-3 index leads to the speculation that IOD is independent of ENSO (Saji et al. 1999; also see Fischer et al. 2005). Using observational data, Saji and Yamagata (2003) found that IOD may result from local air–sea interactions within the tropical Indian Ocean, which is independent of ENSO, but may also interact with ENSO. A recent study (Sun et al. 2015)

also showed that the early Indian monsoon activity in the Bay of Bengal during spring may induce equatorial easterly wind anomaly which triggers IODs that are independent of ENSO. However, some modeling studies suggest that IOD is mainly forced by ENSO (e.g., Yu and Lau 2005), providing a viewpoint different from other modeling studies that indicate the existence of IOD without ENSO (e.g., Hong et al. 2008). Consistent with this paradigm, two independent triggers for IOD have been proposed; one related to an anomalous Hadley circulation over the eastern tropical Indian Ocean in the absence of ENSO and the other related to an anomalous Walker circulation associated with ENSO (Fischer et al. 2005).

It has also been argued that the eastern pole of IOD may be more fundamental and important than the western counterpart in the development of IOD (e.g., Annamalai et al. 2003). Annamalai et al. (2003) also suggested that it is the perturbations in the western Pacific warm pool that are the key for triggering IODs. These perturbations are likely induced by ENSO. Using observational data, Hendon (2003) demonstrated that droughts in Indonesia, which often occur during El Niño, lead to cold SST anomalies in the tropical eastern Indian Ocean through local air–sea interaction. This study aims to explore the validity of this particular mechanism through the analysis of coupled model simulations, but in the absence of ENSO.

The analysis in this paper is based on two 500-year model simulations. The first one is a fully coupled run that retains the ENSO mode of variability (referred to as ENSO run hereafter). In the second run, model predicted daily SST in the tropical Pacific is relaxed to follow the climatological seasonal cycle of daily SST derived from observations. In this way, the variability in tropical Pacific SST, which is dominated by ENSO, is removed from the model integration (referred to as no-ENSO run hereafter). As a first step to better understand IOD variability in isolation, this study focuses on the analysis of the no-ENSO simulation. The main goals of the analysis are (1) to clarify whether ENSO is fundamental to IOD, (2) to explore how changes in Indonesian rainfall can initiate IOD in the absence of ENSO, and (3) to compare the effect of local air–sea feedback with the influence of subsurface ocean dynamics on the development and evolution of IOD.

These goals are achieved by the analysis focused on three base time series, which characterize the variability of Indonesian rainfall, eastern tropical Indian Ocean SST and sea surface height (SSH), respectively. The interaction between the rainfall and SST reflects the local air–sea feedback, whereas the SSH index represents the slow ocean dynamics related to the delayed oscillator. Specifically, the western-boundary-generated Kelvin wave arrives in the eastern Indian Ocean in boreal spring (Rao et al. 2002; Yamagata et al. 2004; Rao and Behera 2005; McPhaden

and Nagura 2014). The change in springtime SSH in the eastern Indian Ocean likely represents the SSH anomalies associated with the Kelvin wave, and thereby, is directly related to the delayed oscillator mechanism. By comparing the relationship between the SST and rainfall indices with that of the SST and SSH indices, the roles played by both the local air–sea interaction and the slow ocean dynamics in the evolution of IOD are elucidated.

Behera et al. (2006) conducted two similar experiments, one of which is a fully coupled simulation and the other is a simulation decoupled in the tropical Pacific sector. The latter is similar to the no-ENSO run in our study with the ENSO variability suppressed. It was found that in the absence of ENSO, IOD can be generated by intrinsic processes within the tropical Indian Ocean (Behera et al. 2006). The present work complements the previous studies, such as Behera et al. (2006), by investigating a specific triggering mechanism of IOD proposed in Hendon (2003) but also in the absence of ENSO and addresses the following questions: what are the characteristics of IOD without ENSO, including the relationships between the eastern and western poles at both the surface and subsurface? And what is their seasonality? How does Indonesian rainfall influence the tropical eastern Indian Ocean SST in the absence of ENSO and act as a trigger for IOD? Can Bjerknes feedback and the delayed oscillator also operate in the evolution of IOD with the removal of ENSO?

This paper is organized as follows. Section 2 provides brief descriptions of the data and model used, as well as experimental design. For the no-ENSO run the evolution of IOD is examined in Sect. 3, including the relationship between surface and subsurface dipoles, the onset of IOD, the influence of initial phases of surface and subsurface anomalies, and the evolution of IOD accompanied by oceanic Kelvin and Rossby waves. Conclusions are given in Sect. 4.

2 Data and model simulations

The data used in this study include model simulations, as well as two ocean reanalysis datasets from the Global Ocean Data Assimilation System (GODAS; Behringer and Xue 2004) on a $0.333^\circ \times 1^\circ$ (latitude \times longitude) grid and the Simple Ocean Data Assimilation (SODA; Carton et al. 2000) version 2.2.4 on a $0.5^\circ \times 0.5^\circ$ grid. Both analysis systems have 40 layers from 5 m below sea level to 4478 and 5375 m depths, respectively, with 20 layers in the upper 200 and 580 m. GODAS and SODA monthly mean SST and SSH from 1981 to 2010 are used as observations to validate the model simulations.

To assess the mean state of the coupled model, monthly mean 10-m wind and precipitation from observations are

also employed. They are taken from the National Centers for Environmental Prediction/Department of Energy (NCEP/DOE) Reanalysis 2 (R2; Kanamitsu et al. 2002) and the Climate Prediction Center Merged Analysis of Precipitation (CMAP; Xie and Arkin 1997), respectively, on a T62 Gaussian grid and a $2.5^\circ \times 2.5^\circ$ grid. Both data from 1981 to 2010 are used.

The model data are from the simulations with the NCEP Climate Forecast System (CFS) version 1 coupled model (Saha et al. 2006). The atmospheric, oceanic, and land components of CFS are the NCEP Global Forecast System (GFS) version 1 (Moorthi et al. 2001), the Geophysical Fluid Dynamics Laboratory (GFDL) Modular Ocean Model version 3 (MOM3; Pacanowski and Griffies 1998), and the Oregon State University (OSU) land surface model (LSM; Pan and Mahrt 1987), respectively.

In this version of CFS, the atmospheric GFS has a horizontal resolution of T62 and 64 vertical levels. The GFDL MOM3 covers global oceans from 74°S to 64°N , with horizontal resolutions of 1° (longitude) by $1/3^\circ$ (latitude) between 10°S and 10°N , and increasing to 1° (latitude) poleward of 30°S and 30°N . Same as GODAS, the ocean model has 40 layers from 5 m below sea level down to 4478 m, with a 10-m resolution in the upper 240 m. The OSU LSM has two soil layers, 0–10 and 10–190 cm. More detailed descriptions of CFS can be found in Saha et al. (2006).

The coupled model was integrated over 500 years for both the ENSO run and no-ENSO run. The ENSO run is a coupled simulation which allows full air–sea interaction over the global oceans and simulates ENSO variability. In the no-ENSO run, the ENSO SST variability is suppressed by assimilating the daily SST climatology into CFS in the tropical Pacific domain (140°E – 75°W , 10°S – 10°N). This was achieved by replacing the model predicted SST in this region with a new SST (SST_{new}) after 1 day of coupled model integration. The new SST is a combination of the model SST predicted by MOM3 (SST_{MOM3}) and observed daily SST climatology (SST_{OBS}) based on the following equation:

$$SST_{\text{new}} = (1-w) \times SST_{\text{MOM3}} + w \times SST_{\text{OBS}},$$

where w is a weighting coefficient, and is set to $1/3$ in the tropical Pacific domain (140°E – 75°W , 10°S – 10°N) and is linearly reduced to 0 on the border of an extended domain (130°E – 65°W , 15°S – 15°N). The observed daily SST climatology was interpolated from the long-term mean monthly SST derived from the NOAA Optimum Interpolation SST (OISST) V2 (Reynolds et al. 2002) over the 1981–2008 period. The use of SST_{OBS} with $w = 1/3$ is equivalent to relaxing the model-simulated SST to the observed climatology with an e-folding time of 3.3 days, which effectively removes the interannual variability of SST in the tropical

Pacific, including El Niño and La Niña. Previously, this set of two 500-year simulations has been used to examine the ENSO variability (Kim et al. 2012), the Pacific decadal oscillation (PDO; Wang et al. 2012a; Kumar et al. 2013), and the impacts of ENSO on PDO (Wang et al. 2012b) and U.S. Southwest drought (Wang and Kumar 2015).

The analysis presented in this paper focuses on the last 480 years of the no-ENSO run. As shown in the next section, without the ENSO timescale variability, some basic characteristics of IOD are well reproduced, suggesting that IOD may exist independent of ENSO. The analysis of IOD based solely on the no-ENSO simulation, therefore, may shed some light on the fundamental aspects of IOD variability. The modulation of IOD by ENSO will be assessed in a subsequent paper via a comparison between the ENSO run and no-ENSO run.

Similar to previous studies (e.g., Saji et al. 1999), the surface IOD is defined as the difference between the SST anomalies averaged over the tropical eastern Indian Ocean (EIO; 90°–110°E, 10°S–Eq.) and western Indian Ocean (WIO; 50°–70°E, 10°S–10°N). The SSH data are employed as a proxy for subsurface heat content (e.g., McPhaden and Nagura 2014), which also represents the variability of thermocline and subsurface temperatures. Similar to the EIO and WIO SST indices, two SSH indices are constructed by averaging the SSH anomalies over the EIO and WIO domains to characterize the subsurface dipole. The correlation between the SST and SSH indices is thus an indicator of the link between the surface and subsurface dipoles.

In addition to monthly mean data, data averaged over different 3-month periods are also used for different seasons. They are March–April–May (MAM) for boreal spring, June–July–August (JJA) for summer, September–October–November (SON) for fall, and December–January–February (DJF) for winter.

3 Results

3.1 Comparison between the mean states of the simulations and observations

Prior to presenting the analysis for IOD, the mean state of the no-ENSO simulation is compared with that of the observations. Figure 1 shows the seasonal mean climatology of SST, 10-m wind and precipitation for MAM, JJA, and SON, respectively, derived from both the no-ENSO run and observations. Overall, the model simulates the seasonal changes in large-scale circulation reasonably well, including Indian summer monsoon precipitation and the associated cross-equatorial flow (Fig. 1b, e).

Some biases in the mean state are also obvious. The modeled SSTs in the northern Indian Ocean and western

Pacific between 10°N and 20°N are colder, especially during spring (Fig. 1a, d). The 10-m zonal wind over the tropical Indian Ocean is generally weaker in the model than in the observations (e.g., Fig. 1a, d). Such an easterly bias is also found in many coupled models (Lee et al. 2013), which may lead to thermocline biases and thus affect Kelvin wave dynamics (Nagura et al. 2013). The no-ENSO run also suffers from the biases in precipitation that are common in many coupled models with rainfall deficit over Indian and excess rainfall over the western Indian Ocean and Indonesia during the monsoon season (Sperber et al. 2012). Since the CFS has the same mean biases as other coupled models, the results in the current study are not likely to be highly model-dependent.

Additionally, in the no-ENSO run, the tropical Pacific SST is nudged towards the observed SST climatology. Since model SST usually has mean biases as compared to observations, the nudging towards the observed mean SST may lead to erroneous simulation of the tropical atmospheric circulation and the Indian Ocean mean state. To address this issue, we compare the mean state of the no-ENSO run (Fig. 1, left panels) with that of the ENSO run (not shown). It is found that the mean states in the two simulations are very similar. The nudging towards the observed SST, therefore, has little influence on the model climatology over the tropical Indian Ocean.

3.2 Relationship between surface and subsurface IODs

The relationships between the surface and subsurface dipoles and that between the two poles of SST/SSH in EIO and WIO are examined first. Figure 2 shows the correlations between the pair of different combinations of the EIO/WIO SST/SSH indices derived from both the no-ENSO run and ENSO run, as well as GODAS and SODA, for each month. For a fair comparison with the 30-year observations, the 480-year model outputs are divided into 16 segments of 30-year period each. The 16-member average of the correlations for individual 30-year segments is compared with the observations. Overall, for each pair of indices, the correlations computed based on the two model runs and the two observational datasets agree well and exhibit similar seasonality (Fig. 2). The correlations in the no-ENSO run are closer to those in the ENSO run and GODAS than in SODA, likely due to the same MOM3 used for both CFS and GODAS.

The relationship between SST and SSH in EIO is characterized by negative correlations in late winter and early spring and positive for the rest of the year with a peak in fall (Fig. 2a). The large spreads during spring among the 16 segments in the no-ENSO run (grey lines) indicate relatively large uncertainty in the relationship between SST and SSH in this season when assessed based on samples

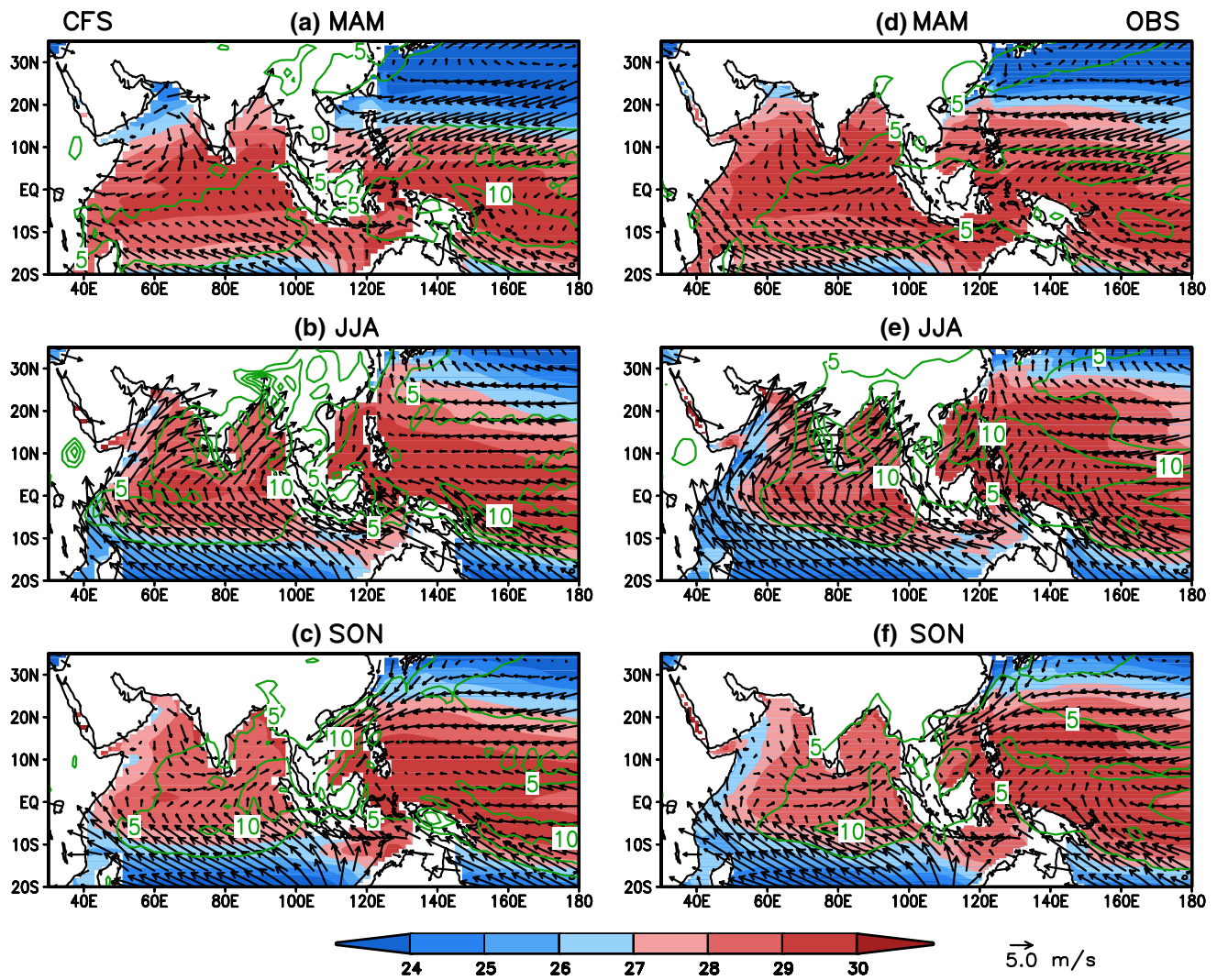


Fig. 1 Seasonal mean climatology of SST (*shading*, unit: °C), 10-m wind (*vector*, unit: m s^{-1}) over oceans, and precipitation (*green contour*, unit: mm day^{-1}) in **a, d** MAM, **b, e** JJA, and **c, f** SON for 480-

year CFS no-ENSO run (*left panels*) and 30-year (1981–2010) observations (*right panels*). The contour interval is 5 mm day^{-1}

of 30-year time series. The negative correlations in the ENSO run, GODAS, and SODA fall within the range of the spreads. For positive correlations, the spreads are small, especially in the peak season. The high correlations (>0.7) during summer and fall suggest a strong connection between the surface and subsurface poles in EIO. Therefore, the slow ocean process is a significant player in the growth and mature phases of IOD.

The correlation between SST and SSH in WIO shows weak seasonality (Fig. 2b) with positive values all year round in the ENSO run, GODAS and SODA. The correlations in the no-ENSO run are small during spring with several members having small negative correlations. This difference between the no-ENSO run and the other three datasets may indicate a modulation of the relationship between SST and SSH in WIO by ENSO. The different

seasonality between Fig. 2a, b suggests that the surface–subsurface interactions in EIO and WIO have different characteristics during the evolution of IOD.

The relationships between the eastern and western poles in the SST and SSH fields are examined in Fig. 2c, d, respectively. The SST anomalies in EIO and WIO are positively correlated in the first half of the year and negatively correlated in the second half (Fig. 2c). Therefore, an SST monopole (Zhao and Nigam 2015) indeed exists in spring, but a dipole appears in summer and fall. With the ENSO variability, the duration of the dipole structure in the SST field seems shorter than without ENSO. In contrast to the surface dipole, the subsurface dipole with an out-of-phase SSH anomaly pattern in EIO and WIO persists through all seasons (Fig. 2d). This, once again, implies different evolutions of IOD in the surface and subsurface.

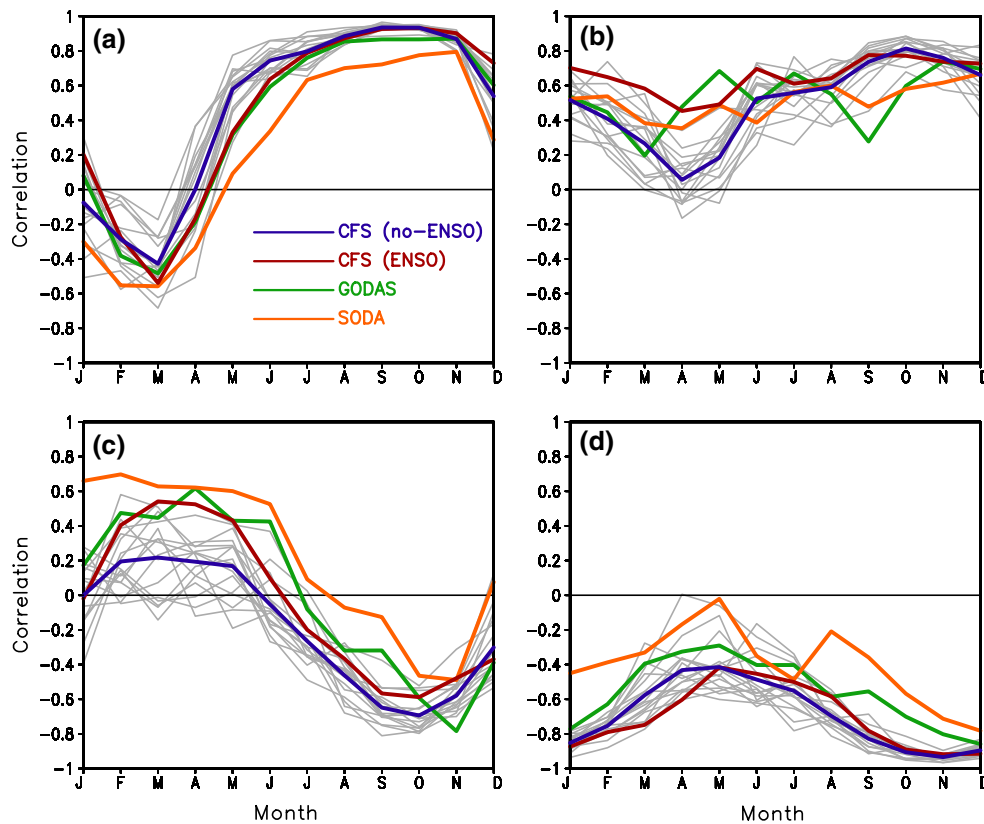


Fig. 2 Correlations between **a** EIO SST and EIO SSH, **b** WIO SST and WIO SSH, **c** EIO SST and WIO SST, and **d** EIO SSH and WIO SSH for each month from January (J) to December (D) with data derived from the 480-year CFS no-ENSO run (blue), 480-year CFS

ENSO run (red), GODAS (1981–2010; green) and SODA (1981–2010; orange). The grey lines are the correlations for 16 individual 30-year segments in the no-ENSO run. The blue (red) line is the average of the 16 members for the no-ENSO (ENSO) run

The strong seasonality of the relationship between SST and SSH in EIO is further documented in Fig. 3, which shows the scatter plot of seasonal mean EIO SST versus EIO SSH for different seasons. In the no-ENSO run (left panels), all points are about evenly distributed among all four quadrants in spring (Fig. 3a), with 109, 114, 127, and 130 points in quadrants I to IV, respectively. During summer (Fig. 3b) and fall (Fig. 3c), the pattern of the points slopes from lower left to upper right. In winter (Fig. 3d), all points tend to return once again to the even distribution across the four quadrants. The scatter plots of the no-ENSO run (Fig. 3, left panels) are similar to those of the ENSO run (not shown) and comparable with GODAS and SODA (Fig. 3, right panels). Figure 3 is consistent with the weak (strong) correlation between EIO SST and SSH in winter and spring (summer and fall) in Fig. 2a. In addition, there is a strong asymmetry in the amplitude between positive and negative EIO SST/SSH anomalies, especially during the peak season (Fig. 3c, g), with larger amplitudes for negative anomalies than for the positive.

The results presented in Figs. 2 and 3 suggest that the no-ENSO run is able to reproduce the realistic association

between the surface and subsurface IODs and its seasonality found in the ENSO run and observations. Therefore, the following analysis focuses on the no-ENSO run to explore some fundamental aspects of the onset and evolution of IOD. The emphasis is placed on EIO as the air–sea coupling is weak in WIO and the western pole is conjectured to be an oceanic dynamical response to the eastern pole (Annamalai et al. 2003; Wajsowicz 2007; Hong et al. 2008).

3.3 Onset of EIO SST anomalies

To explore whether Indonesian rainfall can initiate EIO SST anomalies, similar to Hendon (2003), an Indonesian precipitation (IndoP) index is constructed by averaging precipitation anomalies over the maritime continent within the domain of (95°E–141°E, 10°S–5°N). The region comprises much of Indonesia and part of Malaysia. In the no-ENSO run, the power spectrum of IndoP exhibits most peaks with periods <3 years, whereas in the ENSO run, large peaks are found at the interannual timescale between 3 and 6 years (not shown), indicating a significant modulation of IndoP by ENSO.

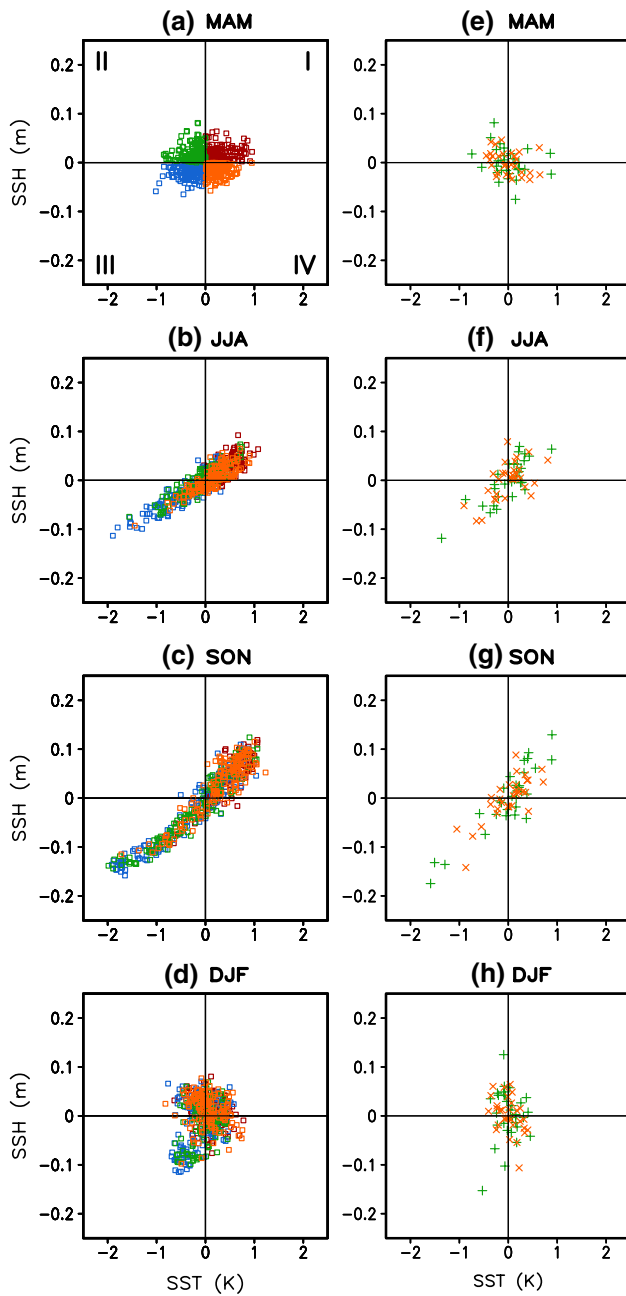


Fig. 3 Scatter plot of seasonal mean EIO SST versus EIO SSH for **a–d** the 480-year no-ENSO run and **e–h** GODAS (green +) and SODA (orange ×). Red, green, blue and orange colors in left panels denote the initial phase of SST and SSH in MAM for the four quadrants (I–IV), respectively

Figure 4 shows the composite evolutions of IndoP, EIO SST, 10-m zonal wind (U10m) and surface net heat flux (HTFL; upward flux >0) averaged over EIO, and WIO SST for positive and negative IOD events, respectively. The composites are based on the positive (negative) IOD events categorized as when SON EIO SST is colder (warmer) than -0.5 K (0.5 K), resulting in a sample size of 120 (148) out of 480.

Associated with the positive phase of IOD (negative EIO SST; Fig. 4a), IndoP decreases from February to April. The IndoP anomaly remains negative until the end of the year. There is a quick adjustment of EIO U10m from a westerly in March to easterly in April, lagging the change in IndoP. The easterly EIO U10m anomaly persists throughout the summer months and is strongly intensified during fall. Driven by the surface wind anomaly, cold EIO SST anomaly gradually grows during late spring and summer and reaches its peak value (over -1 K) in fall, leading to a negative surface heat flux over EIO. For a negative phase of IOD (positive EIO SST; Fig. 4b) the evolution of these anomalies displays similar behavior but with opposite signs.

The composites in Fig. 4 illustrate the onset of IOD via the surface wind response to IndoP, which in turn drives EIO SST. The processes described here in the absence of ENSO are similar to those driven by ENSO as reported in Hendon (2003), Li et al. (2003), and Wang et al. (2003). It is noted that an out-of-phase WIO SST anomaly emerges in June and peaks in October. Its maximum value, however, is about a half of the maximum of EIO SST. The strong intensification of EIO U10m following the peaks of EIO and WIO SSTs likely involves a positive feedback between the zonal wind and zonal SST gradients, i.e., the Bjerknes feedback (e.g., Keenlyside and Latif 2007), as the SST difference between EIO and WIO is largest during fall.

The onset of EIO SST triggered by IndoP is also evident in the lagged relationship between spring IndoP and U10m/SST of the following seasons. Figure 5 shows the lag correlation/regression of SST/10-m wind with MAM IndoP. In spring (Fig. 5a), associated with drier-than-normal precipitation over Indonesia, southeasterly wind anomalies are found off Java and Sumatra. The surface wind pattern favors anomalous upwelling and leads to cold EIO SST (Annamalai et al. 2003), consistent with the negative correlation of SST off Java and Sumatra with $-$ IndoP (Fig. 5a). The SST correlation pattern also agrees well with that based on observational data (Fig. 5a in Hendon 2003).

In summer (Fig. 5b), both lagged correlation of SST and lagged regression of 10-m wind with MAM IndoP are stronger, suggesting a wind/SST response to IndoP. The anti-cyclonic circulation to the southwest of tropical cooling associated with $-$ IndoP indicates a Gill-type response (Gill 1980). Weak but positive correlations of SST show up in WIO, consistent with the emergence of the out-of-phase WIO SST during summer (Fig. 4). In fall (Fig. 5c), both the positive SST correlation and equatorial easterly wind anomalies become stronger. This is consistent with the strong intensification of EIO U10m during fall found in Fig. 4. In the peak season of IOD, surface easterly wind anomalies over the equatorial Indian Ocean are strongly enhanced due to a well-established zonal SST

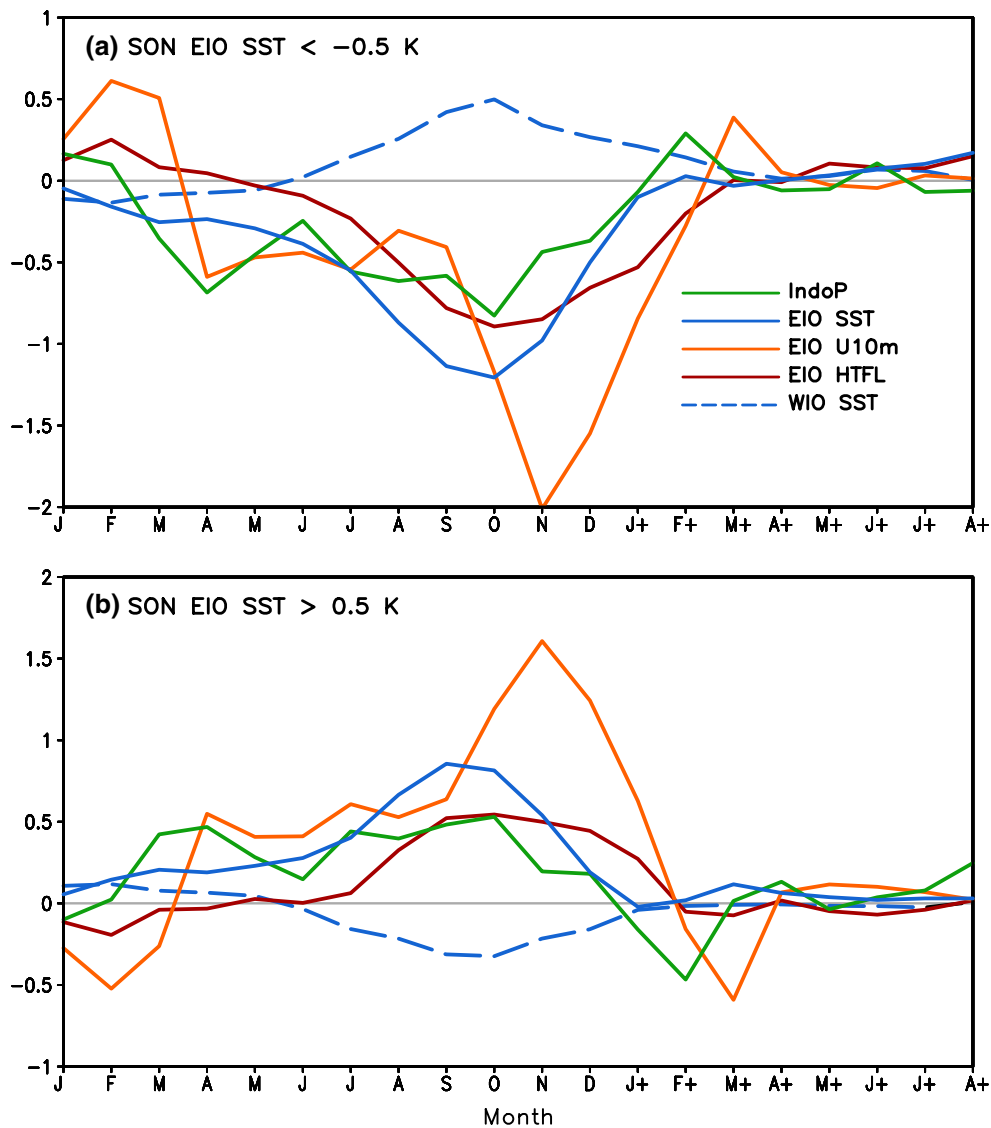


Fig. 4 Composites of Indonesian precipitation (IndoP, green, mm day^{-1}), EIO SST (blue, K), EIO 10-m zonal wind (U10m, orange, m s^{-1}), EIO net surface heat flux (HTFL, red, 50 W m^{-2}),

and WIO SST (blue dash, K) anomalies for SON EIO SST **a** colder than -0.5 K and **b** warmer than 0.5 K , respectively, from January (J) to the August of following year (A+)

gradient between EIO and WIO, i.e., the process of Bjerknes feedback.

The evolution of IOD also involves an interaction between the surface and subsurface in summer and fall. Figure 6 presents the simultaneous correlation/regression of SSH/10-m wind against the negative of EIO SST for the two seasons, respectively. There are negative correlations of SSH in EIO and positive correlations in WIO in both seasons. Associated with cold EIO SST, the thermocline is shallow in EIO and deep in WIO with warm WIO SST. Together with the southeasterly wind anomalies off Java and Sumatra, the change in EIO SSH tends to strengthen the already cold EIO SST. The zonal component of the surface wind is then further enhanced by the strengthening

of zonal SST gradient associated with the development of IOD, which, in turn, reinforces the variations of the thermocline. Therefore, after the initiation of EIO SST by IndoP in spring, EIO SST may grow through Bjerknes feedback in summer and fall (e.g., Annamalai et al. 2003). The strengthening of both correlation and regression coefficients from summer to fall indicates that the interactions among surface wind, SST, and SSH are the result of a positive feedback.

3.4 Influence of initial phases of EIO SST and SSH

It is noted in Fig. 3 that the phases of EIO SST and EIO SSH in spring are almost equally distributed among the

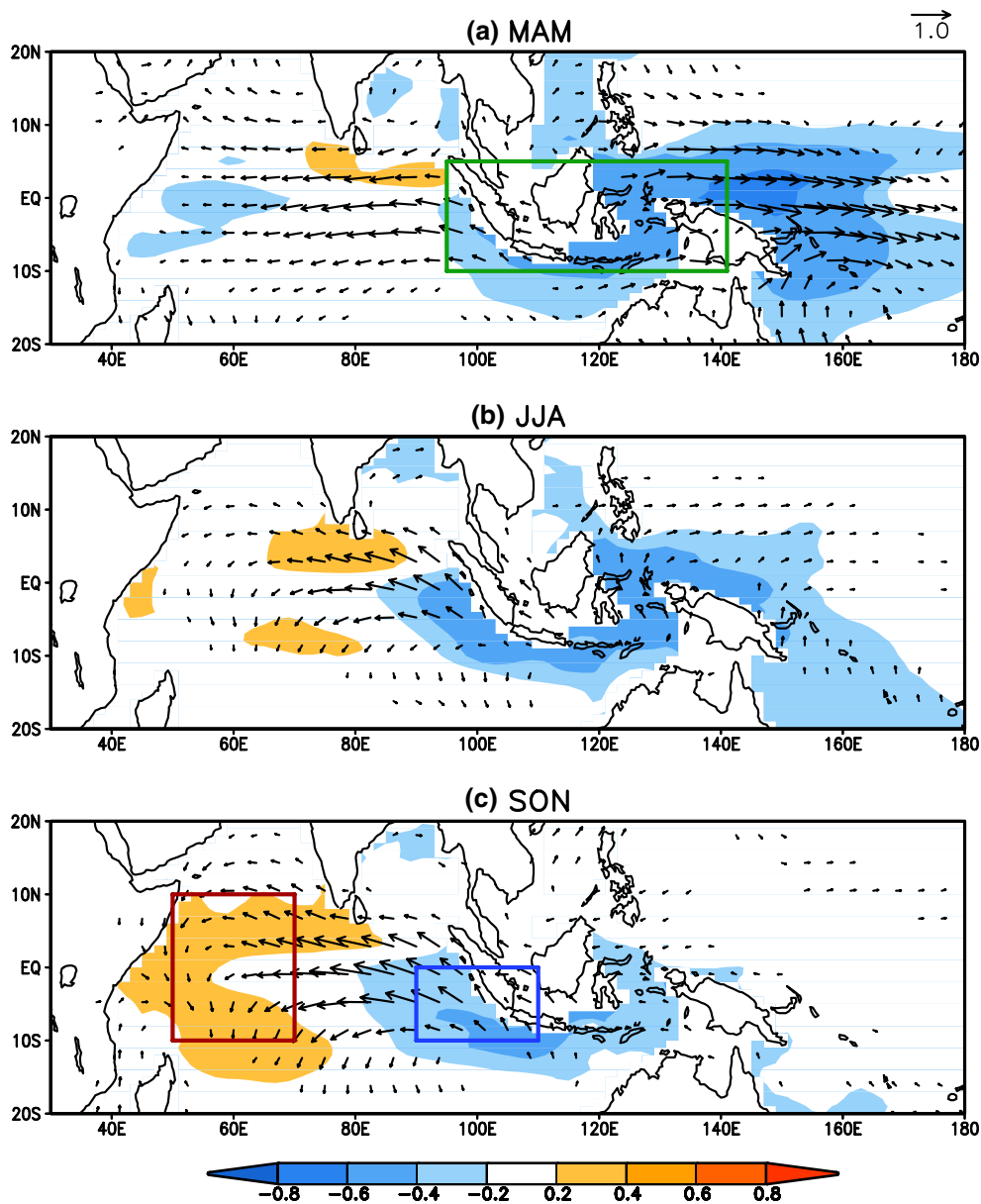


Fig. 5 Correlation of SST (*shadings*) and regression of 10-m wind (*vectors*, m s^{-1}) against the negative of MAM IndoP for **a** MAM, **b** JJA, and **c** SON seasonal mean SST and 10-m wind over the 480 years. The correlation coefficients with *shadings* are above the 99 % significance level estimated by the two-tailed *t* test. The regression coefficients of 10-m wind are associated with -1 mm day^{-1} of

IndoP. The wind vectors with magnitudes $<0.1 \text{ m s}^{-1}$ are omitted. The *green box* in (a) denotes the domain within which precipitation anomalies are averaged over the maritime continent for IndoP. The *blue* and *red boxes* in (c) denote the EIO and WIO regions used for averaging SST

four quadrants, whereas in summer and fall they tend to be confined in quadrants I and III. The latter is consistent with the strong link between SST and SSH in EIO during the developing and mature stages of IOD (Figs. 2a, 6). The correlations of SON EIO SST with MAM EIO SST and MAM EIO SSH are 0.54 and 0.16, respectively. This implies that 29 % of the peak season EIO SST variance can be explained by springtime EIO SST, but $<3 \%$ can be explained by EIO SSH. Therefore, MAM EIO SST is

a better predictor for IOD than MAM EIO SSH. However, the phase of MAM EIO SSH relative to MAM EIO SST also plays a role in determining the growth of EIO SST, and thus contributes to the predictability of IOD.

How the initial phase of EIO SSH in spring affects the development of EIO SST in the following seasons is further examined. Figure 7 shows the composite evolutions of EIO SST and EIO SSH conditional upon the phases of EIO SST and SSH in spring. Only the years with the amplitudes of

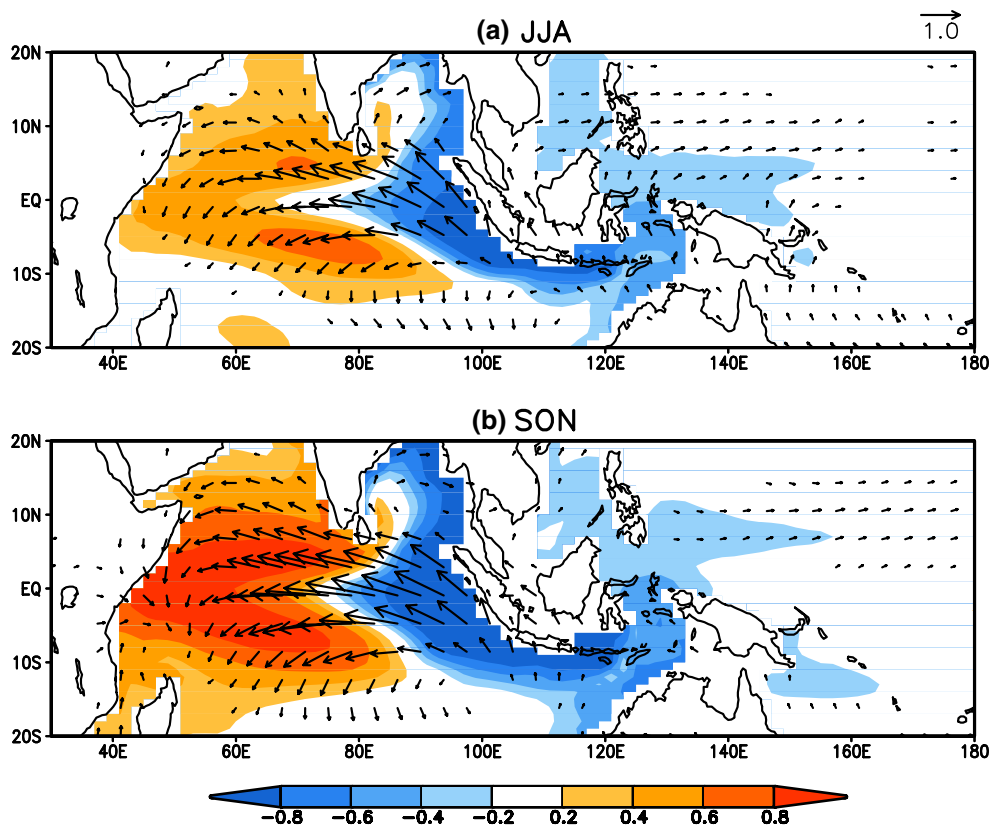


Fig. 6 Simultaneous correlation of SSH (*shadings*) and regression of 10-m wind (*vectors*, m s^{-1}) against the negative of EIO SST for **a** JJA and **b** SON over the 480 years. The correlation coefficients with *shadings* are above the 99 % significance level estimated by the

two-tailed t test. The regression coefficients of 10-m wind are associated with -0.5 K of EIO SST. The wind vectors with magnitudes <0.1 m s^{-1} are omitted

MAM EIO SST > 0.2 K and MAM EIO SSH > 0.01 m are selected for the composites. Although negative (positive) EIO SST anomalies in fall stem mostly from the same-sign MAM EIO SST in quadrants II and III (I and IV), the growth of EIO SST is influenced by the sign of EIO SSH. When EIO SST (Fig. 7a) and EIO SSH (Fig. 7b) are out of phase in spring, the development of EIO SST is suppressed in late spring and early summer (Fig. 7a; green and orange lines). Consequently, the corresponding peak value in fall is less than that when springtime EIO SST and SSH are in phase (Fig. 7a; blue and red lines).

The initial phases of EIO SST and SSH affect not only the growth of EIO SST but also the response of SST and 10-m wind to Indonesian rainfall. Figure 8 shows the lag correlation/regression of SST/10-m wind with the negative of MAM IndoP over the years when MAM EIO SST and SSH are in phase (quadrants I and III; left panels) and out of phase (quadrants II and IV; right panels), respectively. Compared to the analysis over the entire 480 years (Fig. 5), the SST correlation and 10-m wind regression coefficients are much larger in Fig. 8a–c and smaller in Fig. 8d–f. There is a strong response of 10-m wind to springtime Indonesian

rainfall, as well as strong air–sea coupling, when MAM EIO SST is in phase with EIO SSH. In contrast, the response is much weaker when MAM EIO SST and SSH are out of phase.

To illustrate how the local air–sea interaction and slow ocean dynamics affect the evolution of IOD, Figs. 9 and 10 show lead-lag correlations of EIO SST with IndoP and EIO SSH, respectively, over the 480 years as well as over the years when MAM EIO SST and SSH are in phase (quadrants I and III) and out of phase (quadrants II and IV). Significant correlations with springtime IndoP are found for EIO SST leading by 2 months and lagging up to 8 months (Fig. 9a). The maximum correlations at -1 and $1-3$ months indicate a response of IndoP to EIO SST with a 1-month delay and a response of EIO SST to IndoP with longer delays. During late summer and early fall, there are significant correlations for EIO SST lagging IndoP, suggesting primarily an SST response to IndoP in its developing phase. In late fall, EIO SST also feeds back to IndoP, manifested by increasing correlations for SST leading IndoP.

For the in-phase MAM EIO SST and SSH, the interactions between EIO SST and IndoP are largely enhanced

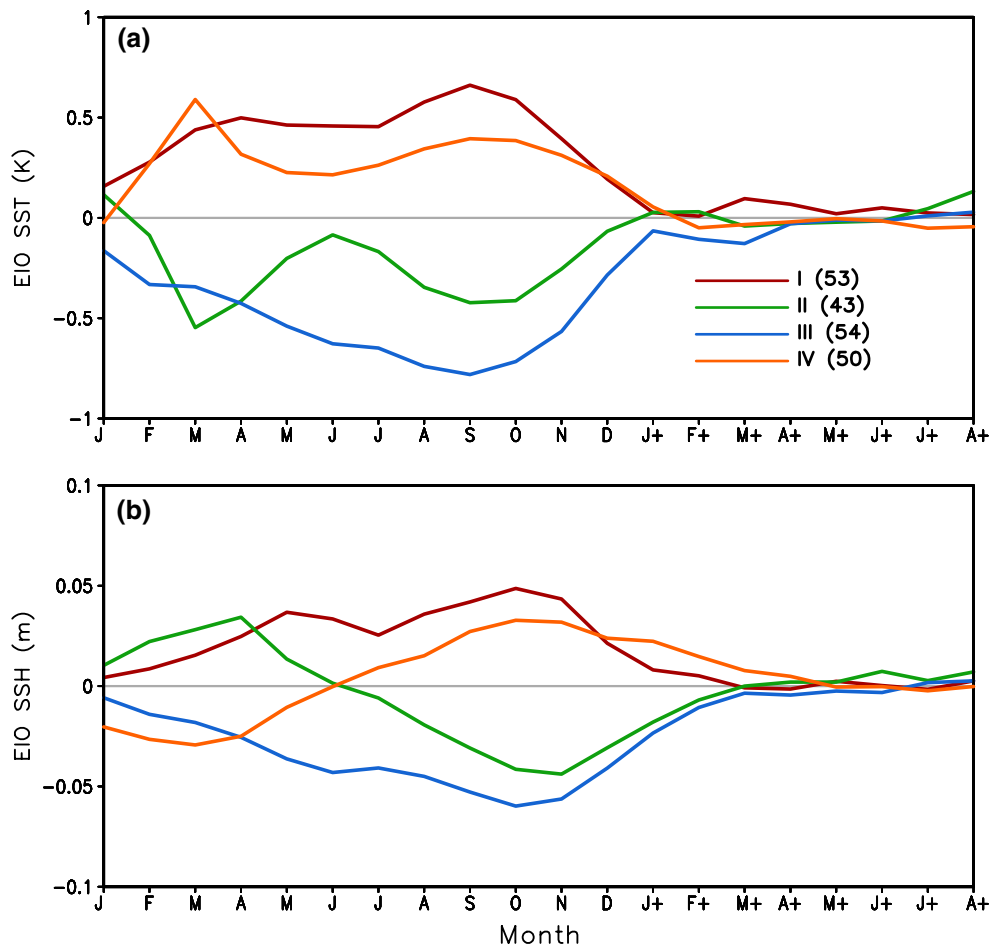


Fig. 7 Composites of **a** EIO SST (K) and **b** EIO SSH (m) from January (J) to the August of following year (A+) for the initial phase of the pair of MAM EIO SST and SSH (Fig. 2a) in quadrants I (red), II (green), III (blue), and IV (orange), respectively. Only the years

with the amplitudes of MAM EIO SST > 0.2 K and MAM EIO SSH > 0.01 m are selected for the composites. The number of years selected for each quadrant is listed in parentheses

(Fig. 9b). Particularly, there are significant positive correlations for both SST leading and lagging summer IndoP, implying a positive feedback between SST and precipitation. In addition, the SST correlations with IndoP extend to longer leads and lags, which is another indicator of the enhanced SST–IndoP interaction. When MAM EIO SST and SSH are out of phase, the correlations between EIO SST and IndoP are significantly reduced (Fig. 9c) as compared to Fig. 9a, especially for SST lagging IndoP. The SST response to IndoP is considerably weakened in this case.

The lead-lag correlations between EIO SST and EIO SSH are characterized by weak correlations in spring and strong positive correlations for both SST lagging summer SSH and SST leading fall SSH (Fig. 10a). The results suggest an SST response to the change in summer SSH, which in turn affects SSH in fall. The processes are consistent with Bjerknes feedback during summer and fall depicted in

Fig. 6. When MAM EIO SST and SSH are in phase, their positive feedback can occur as early as in spring months (Fig. 10b). On the other hand, when EIO SST and SSH are opposite, the positive correlations become relatively weak with a significant delay (Fig. 10c). Therefore, the initial phases of EIO SST and SSH are important in determining the surface–subsurface interaction in the following summer and fall. Additionally, the correlations in Fig. 10 are higher than those in Fig. 9, especially in summer and fall, suggesting an overall stronger association between EIO SST and SSH than the association of EIO SST with IndoP. The results indicate the importance of the ocean subsurface process in the development of IOD, as well as the importance of the local air–sea feedback in the initiation of IOD. The information about both springtime Indonesian precipitation and EIO thermocline is likely crucial for the prediction of IOD.

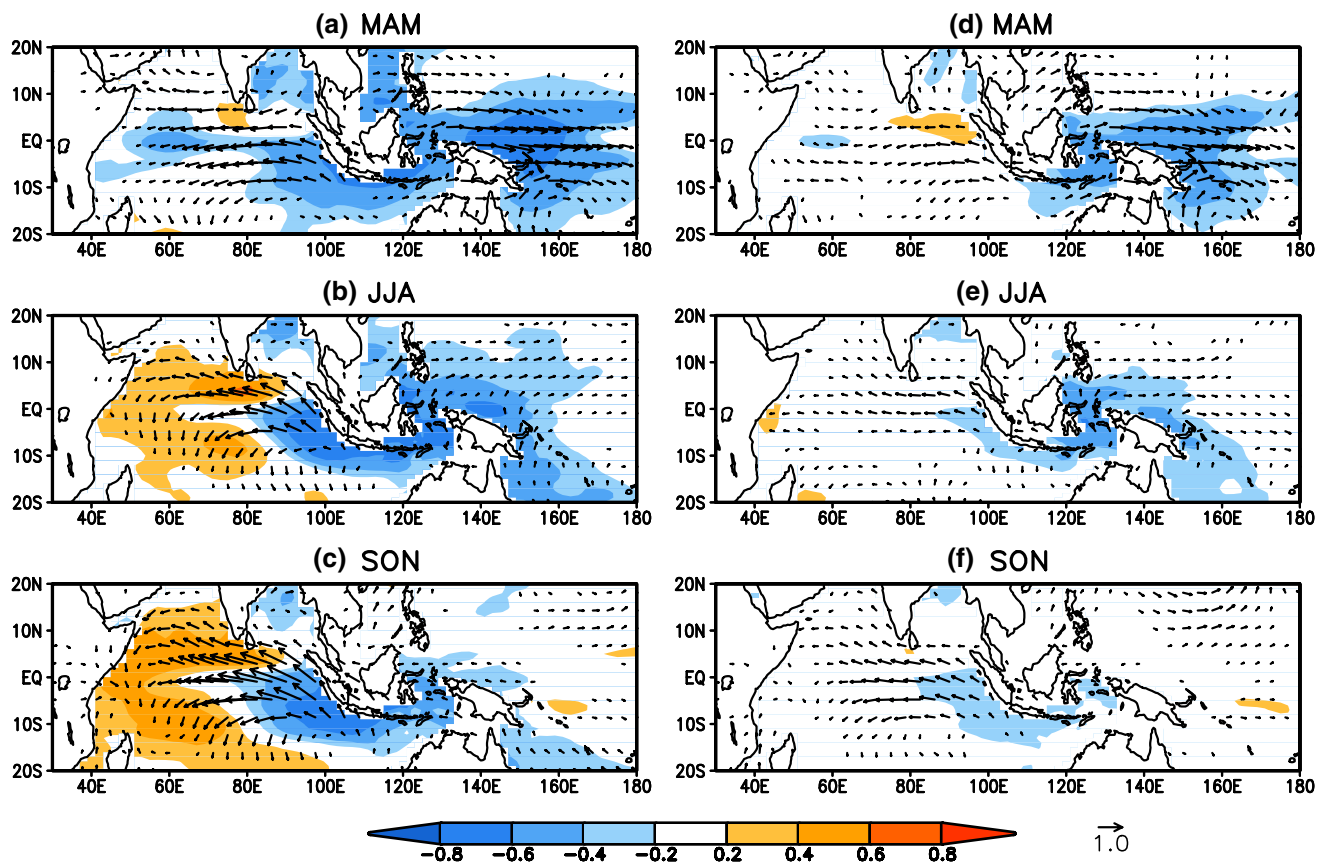


Fig. 8 Same as Fig. 4 but over years when MAM EIO SST and EIO SSH are **a, b, c** in phase (quadrants I and III in Fig. 2a) and **d, e, f** out of phase (quadrants II and IV in Fig. 2a). Also similar to Fig. 6,

only the years with the amplitudes of MAM EIO SST > 0.2 K and MAM EIO SSH > 0.01 m are selected for the correlation/regression analysis

3.5 Evolution of IOD

The extended empirical orthogonal function (EEOF) technique (Weare and Nasstrom 1982) is used to illustrate the evolution of IOD together with the subsurface ocean temperature anomalies. The EEOF analysis is based on the spatial and temporal covariance matrix of 480-year monthly tropical ocean temperature averaged between 10°S and 5°N with a window length of 9 months. The longitude–depth domain used for the analysis is from 50°E to 110°E over the tropical Indian Ocean and from the 5-m depth (top layer of the ocean model; taken as sea surface) to the 225-m depth below the surface.

Although the thermocline movement associated with IOD has been described by many previous studies (e.g., Feng et al. 2001; Huang and Kinter 2002; Rao et al. 2002; Feng and Meyers 2003; Yamagata et al. 2004; Rao and Behera 2005; McPhaden and Nagura 2014), the results presented here differ from the existing studies in the following aspects: (1) the EEOF analysis indicates two modes related to the evolution of IOD, one stationary and the other non-stationary; (2) the EEOF modes exhibit the

vertical structure of subsurface temperature associated with the evolution of IOD; (3) both spatial and temporal evolution of IOD can be inferred from the lead-lag relationship between the time series of the two modes; and (4) the evolution of IOD is shown in the absence of ENSO.

Figure 11 displays the first EEOF mode with correlation/regression maps of mean ocean temperature averaged over 10°S – 5°N against the principal component (PC) of EEOF1 from month -2 to month 8, which denote the ocean temperature leading PC1 by 2 months and lagging PC1 by 8 months, respectively. The maps are shown for the entire 480 years (left column), as well as for the years when MAM EIO SST and MAM EIO SSH are in phase (middle column) and out of phase (right column), respectively. This mode accounts for 28 % of tropical Indian Ocean surface–subsurface temperature variance. EEOF1 represents the evolution of IOD with a non-propagating feature (Fig. 11, left column). Cold EIO SST and warm WIO SST anomalies are discernible at month -2 and month 0, respectively, followed by the strengthening of a subsurface dipole, which reaches its peak at month 4. After that, both surface and subsurface IODs enter their decay phase. The

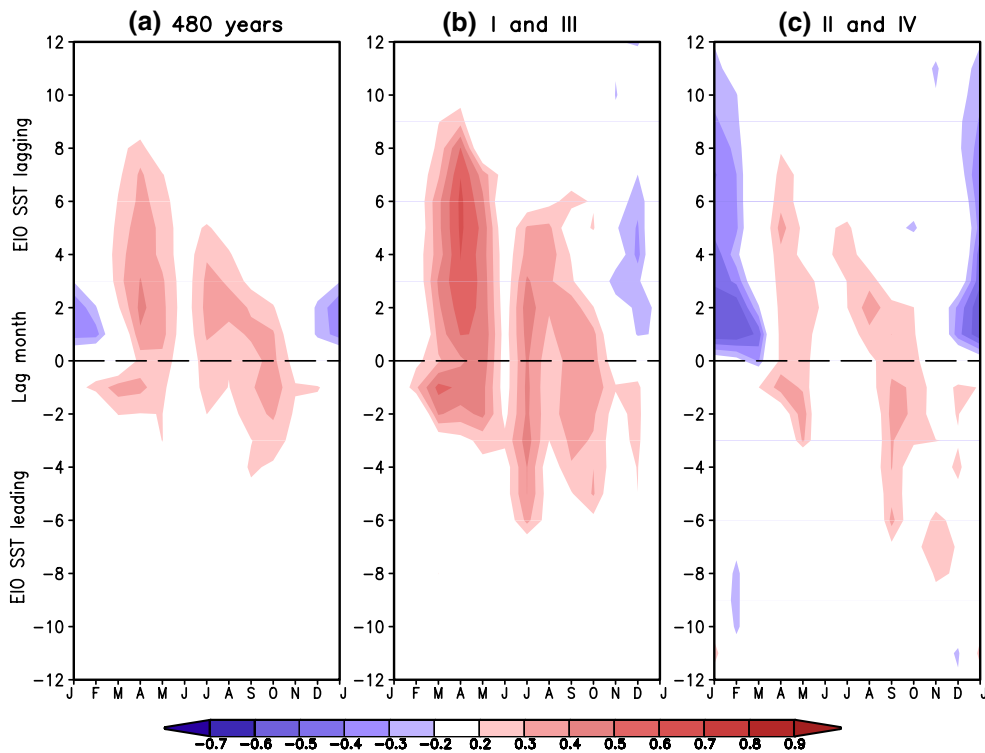


Fig. 9 Lead and lag correlations between EIO SST and IndoP of each month labeled along the x axis over **a** 480 years, years when MAM EIO SST and MAM EIO SSH are **b** in phase, and **c** out of phase. In **b** and **c**, only the years with the amplitudes of MAM EIO

SST > 0.2 K and MAM EIO SSH > 0.01 m are selected for the correlation analysis. The correlations are shown for EIO SST lagging IndoP from -12 months to 12 months. A negative lag means EIO SST leads IndoP

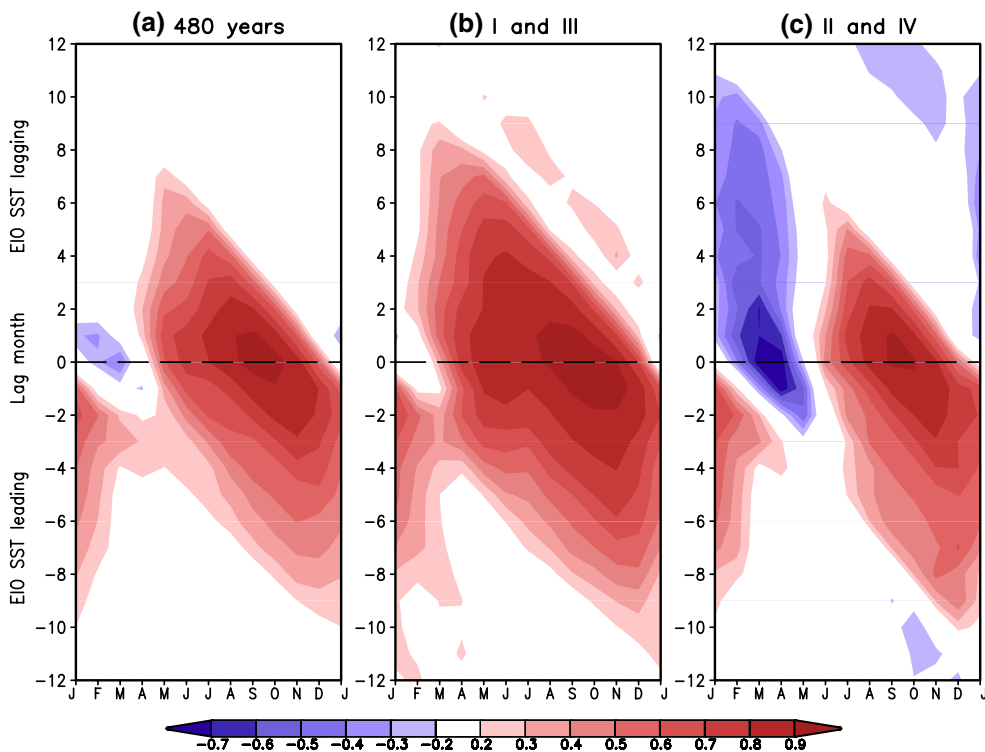
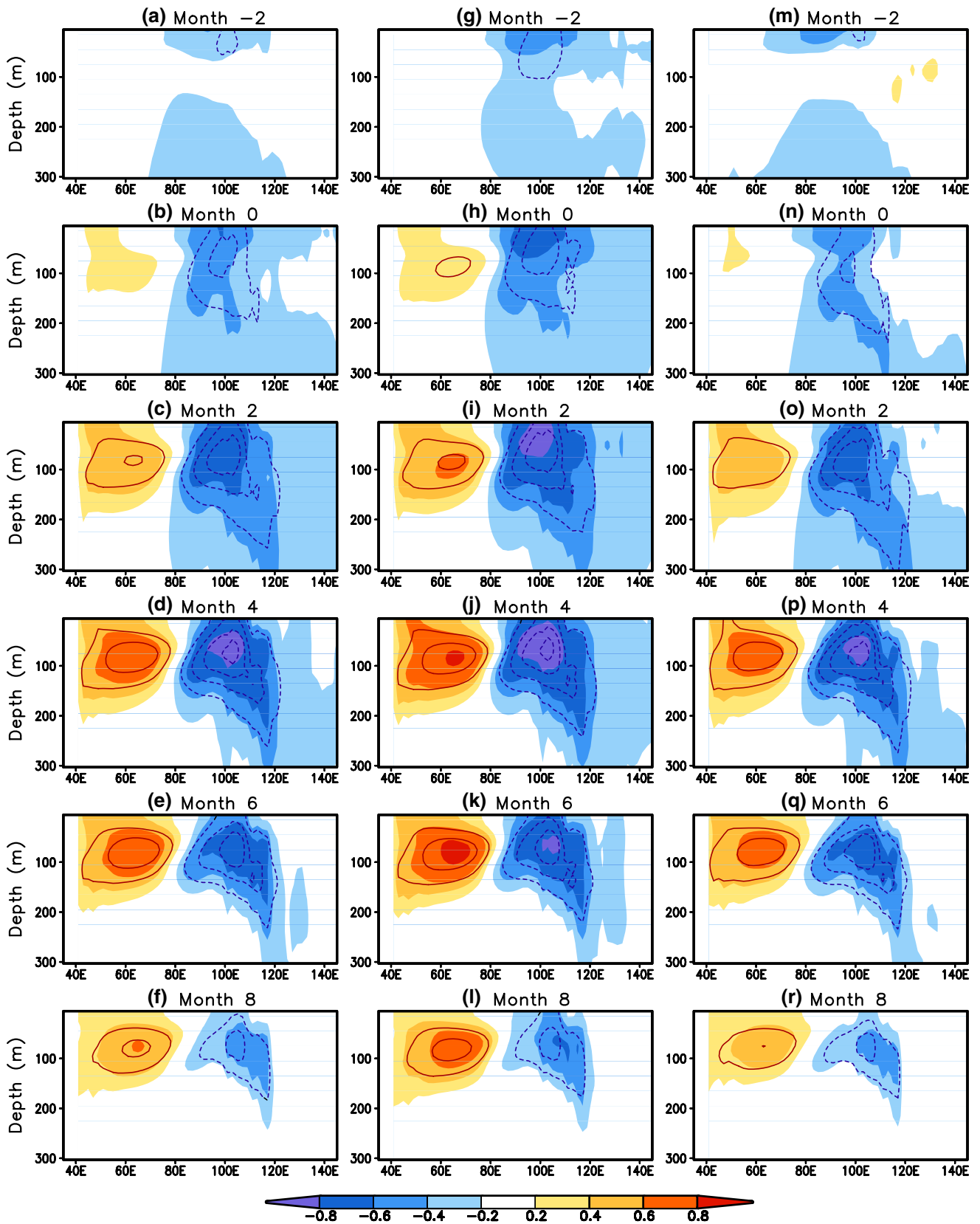


Fig. 10 Same as Fig. 9, but for lead and lag correlations between EIO SST and EIO SSH



◀ **Fig. 11** Correlation (*shading*) and regression (*contour*) of monthly mean ocean temperature averaged over 10°S–5°N against the principal component (PC) of the first EEOF of the 10°S–5°N mean ocean temperature over the domain of 50°E–110°E and 5–225-m depth for **a–f** 480 years, years when MAM EIO SST and MAM EIO SSH are **g–l** in phase, and **m–r** out of phase. Month –2 and month 2 denote ocean temperature leading and lagging PC1 by 2 months, respectively. Contour interval is 0.25 K with negative values dashed and zero contours omitted

surface and subsurface temperature anomalies in EIO are strong and penetrate deep down to 300-m depth. In contrast, the temperature anomalies in WIO are relatively small and shallow.

Comparing the evolutions when MAM EIO SST and SSH are in phase (Fig. 11, middle column) and out of phase (Fig. 11, right column), no significant differences are found between the two in the subsurface. The correlation and regression coefficients are slightly larger when the initial EIO SST and SSH are in phase than out of phase, especially, near the sea surface, which is consistent with Fig. 7a.

The second EEOF accounts for 18 % of tropical Indian Ocean surface–subsurface temperature variance. As shown in Fig. 12 (left column), EEOF2 captures an eastward propagating Kelvin wave that contributes to the evolution of IOD. From month –2 to month 2, a well-defined dipole exists in both the surface and subsurface. As the warm temperature anomalies move eastward in the form of a downwelling Kelvin wave, cold temperature anomalies begin to withdraw from EIO (Fig. 12d). At month 8, a negative IOD is established. The influence of the initial phase difference between EIO SST and SSH (Fig. 12, middle and right columns) is mainly confined to the surface during the months –2 and 2.

Compared to EEOF1 (Fig. 11), the cold EIO temperature anomalies in EEOF2 (Fig. 12) are weak and shallow persisting only for a short duration. Additionally, an upwelling Kelvin wave shoals the thermocline but cooling SSTs requires turbulent kinetic energy to entrain cold water, whereas a downwelling Kelvin wave will deepen the thermocline and warm the SSTs more easily.

To demonstrate the existence of Rossby waves in the subtropical Indian Ocean during the evolution of IOD (e.g., Yamagata et al. 2004; Rao and Behera 2005), an additional EEOF analysis is performed with 9°S–11°S mean ocean temperature in the same longitude–depth domain (50°E–110°E, 5–225-m depth). Figure 13 shows the evolution of the first EEOF in the subtropical southern Indian Ocean, which explains 30 % of the subtropical ocean temperature variance. The downwelling warm temperature anomalies propagate westward, deepen the thermocline and generate warm SST anomalies in WIO. The influence of the phase difference between MAM EIO SST and SSH (Fig. 13, middle and right columns) on the Rossby waves is also discernible, though small.

The PCs of the two equatorial EEOF modes (Figs. 11, 12) are orthogonal with no correlation due to the constraint of orthogonality for the EEOF analysis. However, lagged correlations between the two PCs are nonzero, as shown in Fig. 14 (red line with dots). The largest positive (negative) correlation is found when PC1 leads (lags) PC2 by 4 months. This is the timescale (2×4 months) for an alternation between the two modes during the evolution of IOD. For example, the evolution of an IOD may be first dominated by EEOF1 (Fig. 11). During the developing phase, both the surface and subsurface IODs are intensified from month 0 to month 4 (Fig. 11b–d). After reaching the peak intensity at month 4 (Fig. 11d), EEOF2 may kick in during the decay phase. The evolution of IOD then continues from month 0 in Fig. 12b because there is the largest positive correlation between the two PCs when PC1 leads PC2 by 4 months (Fig. 14, red line) and the two spatial patterns in Figs. 11d and 12b resemble each other. In the following 4 months (Fig. 12c, d), the warming Kelvin wave offsets the cold EIO anomaly with an IOD neutral condition (Fig. 12d). After another 4 months, a negative phase of IOD is established (Fig. 12f), which may continue to evolve but returns to EEOF1 (Fig. 11). The 8 months during which IOD switches from a positive phase to a negative phase coincide with the time interval between the largest positive and negative correlations (Fig. 14, red line).

The contributions of Kelvin and Rossby waves in the evolution of IOD can be inferred from the lagged correlations between PC1 of the subtropical EEOF (Fig. 13) and the two PCs of the tropical EEOFs (Figs. 11, 12), which are also shown in Fig. 14 (blue and green lines with dots). The non-propagating tropical EEOF1 highly correlates with the subtropical EEOF1 with correlations >0.6 when the tropical mode leads the subtropical mode by 0–6 months (Fig. 14; blue line). This suggests that the westward-propagating Rossby wave is generated after the emergence of the wind-driven cold EIO SST in response to IndoP, consistent with the Gill model (Gill 1980). The equatorial Kelvin wave mode correlates with the subtropical Rossby wave mode at both lead and lag months (Fig. 14; green line). The largest negative and positive correlations are found when the Kelvin wave leads the Rossby wave by 9 months and lags by 3 months, respectively. Therefore, it takes about 12 months for the Rossby wave due to the reflection of the Kelvin wave at the eastern boundary to travel across the Indian Ocean basin and then it is reflected into another Kelvin wave at the western boundary. The 12-month interval is consistent with the biennial feature of both IOD (Webster and Hoyos 2010) and Rossby waves in the Indian Ocean (Rao et al. 2002; Gnanaseelan et al. 2008), as well as the seasonal phase-locking of EIO SST (Zhang and Yang 2007). In particular, the modeling study of Behera et al.

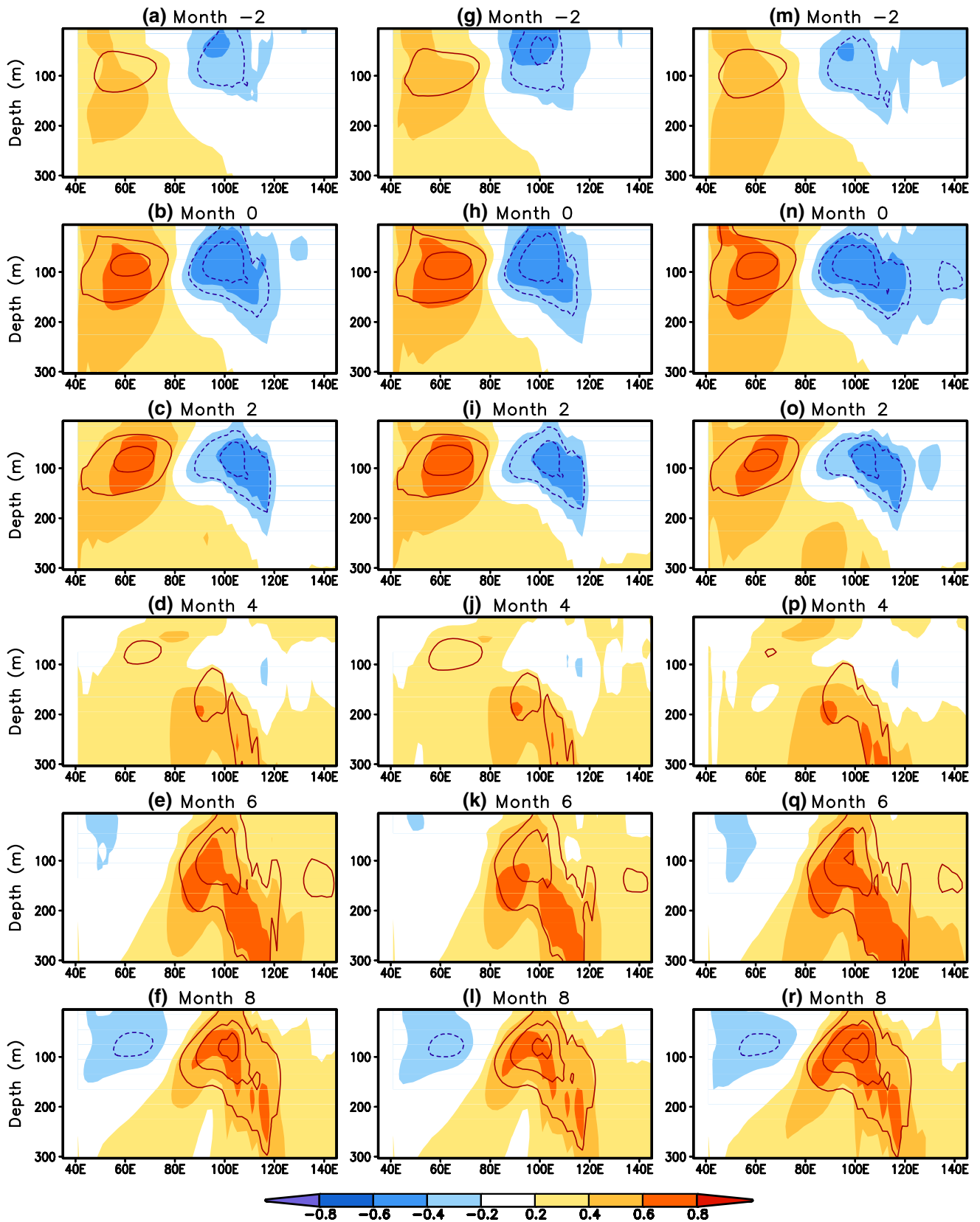


Fig. 12 Same as Fig. 11 but for the second EOF

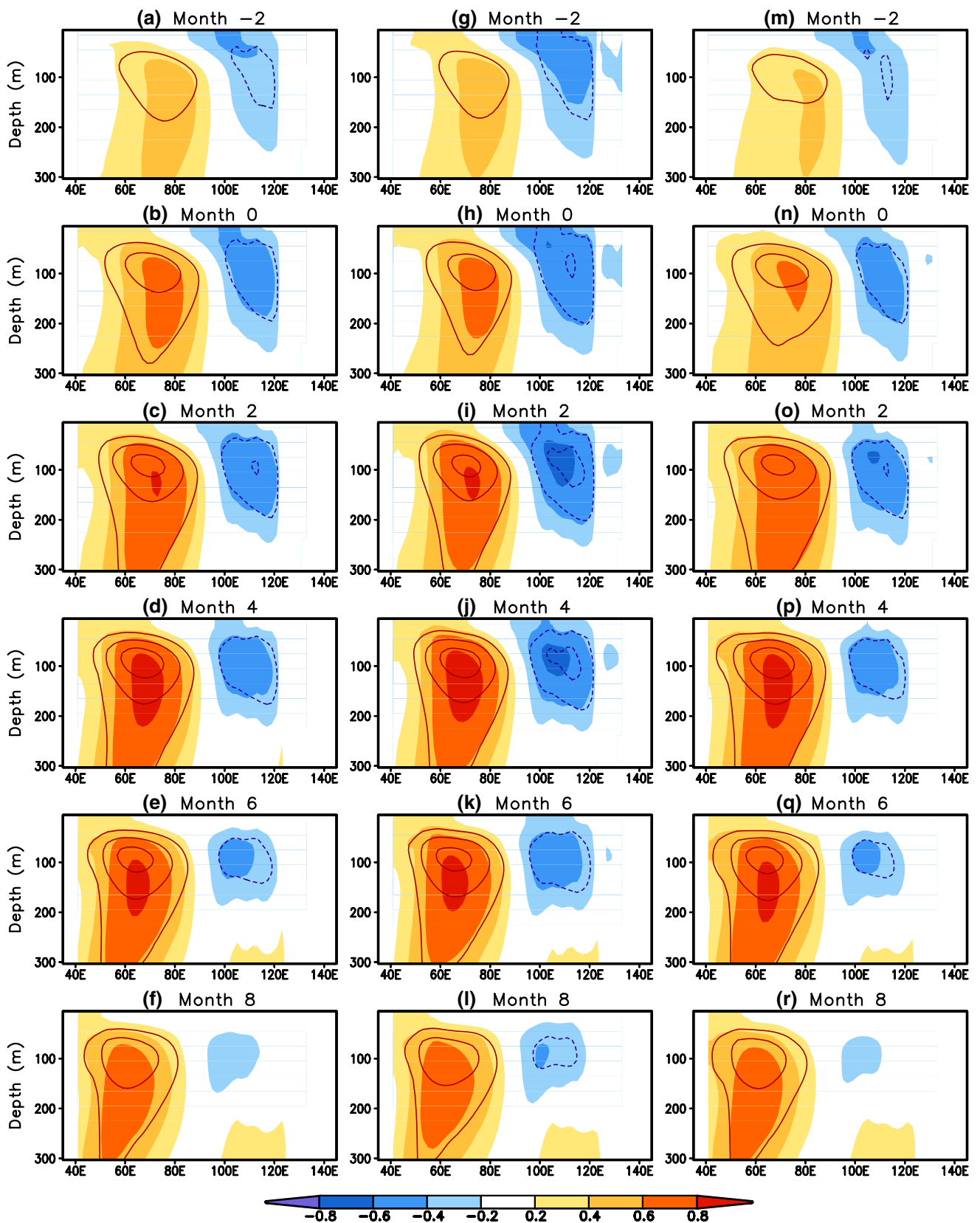


Fig. 13 Same as Fig. 11 but for the first EOF of 480-year monthly mean ocean temperature averaged over 10°S–5°N

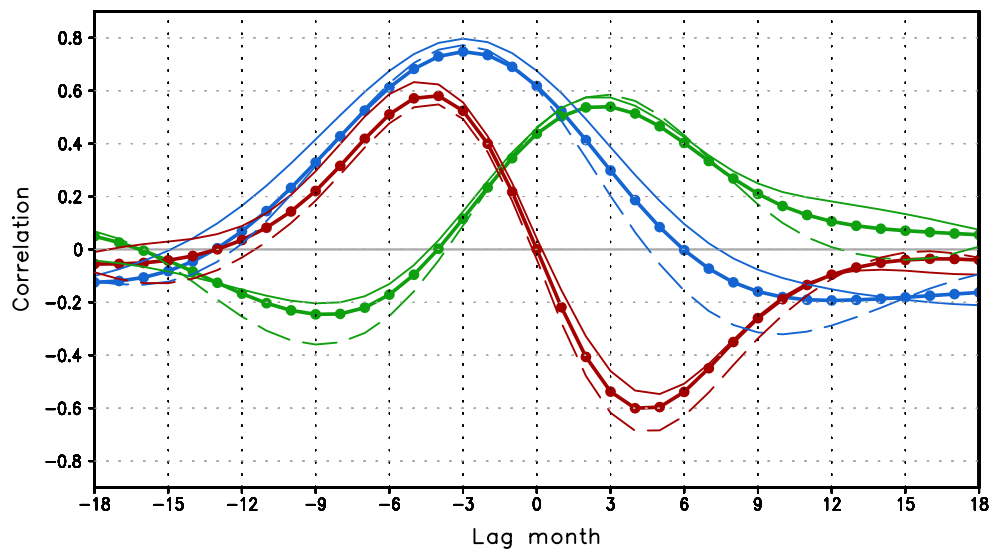


Fig. 14 Lead-lag correlations between PC1 and PC2 of the tropical EEOFs (*red*), between PC1 of the tropical EEOF and PC1 of the subtropical EEOF (*blue*), and between PC2 of the tropical EEOF and PC1 of the subtropical EEOF (*green*) with negative lags denoting the

former leading the latter over the 480 years (*thick solid curve with dots*), years when MAM EIO SST and MAM EIO SSH are in phase (*thin solid curve*), and out of phase (*thin dash curve*), respectively

(2006) illustrates that the interannual variability of IOD is primarily biennial in the absence of ENSO.

The initial phases of MAM EIO SST and SSH also affect the magnitude of the lead and lag correlations (Fig. 14, thin solid and dash lines). However, they don't alter the frequencies of the Kelvin and Rossby waves, or the timing of the transition between the EEOF modes.

Given the forcing mechanisms for the onset and evolution of IOD presented in this paper, it is reasonable to speculate that the seasonality of IOD is closely tied to the characteristics of these forcing factors. For instance, large anomalies of IndoP in spring initiate the eastern pole of IOD and excite a westward-propagating Rossby wave. Both the phase speeds of the Rossby and Kelvin waves and the basin geometry may determine the timing of the growth of the western pole and the decay of the eastern pole, leading to a preferred time scale for IOD. The control of the seasonality of the monsoons around the Indian Ocean, especially that of IndoP, remains to be understood as far as the phase-locking of IOD is concerned.

4 Conclusions

The evolution of IOD and its forcing mechanisms were examined in this study using CFS coupled model simulations with the removal of the ENSO mode of variability. The model can reproduce some observed features of IOD even without ENSO, including the relationships between the eastern and western poles in both the surface and

subsurface, as well as their seasonality. The results indicate that ENSO is not fundamental for the existence of IOD.

It was demonstrated that cold EIO SST anomalies associated with IOD can be initiated by springtime Indonesian rainfall deficit through local surface wind response. The growth of EIO SST anomalies also depends on the initial phase of springtime EIO SSH. Both the air–sea interaction and subsurface variability play a role in the development of IOD via the Bjerknes feedback. This points to the importance of a better prediction of tropical precipitation (Sooraj et al. 2012) and a more realistic modeling of Indian Ocean subsurface (Wang et al. 2013) for improving the seasonal forecast of IOD (Wajsowicz 2007; Shi et al. 2012). Given the strong influence of ENSO on Indonesian precipitation (Aldrian and Susanto 2003; Hendon 2003), an implication is that the Indonesian precipitation can act as a medium linking ENSO and IOD.

The evolution of IOD can be represented by two leading EEOF modes of tropical surface–subsurface ocean temperatures, one stationary and the other non-stationary. The onset, development, and termination of EIO SST, as well as the transition to the opposite phase, can be interpreted as alternations between the two EEOFs with the eastward-propagating Kelvin wave (EEOF2). In the absence of ENSO, the evolution of IOD is also accompanied by westward-propagating Rossby waves depicted by EEOF1 of subtropical surface–subsurface ocean temperatures. The lead and lag correlations between the two PCs of the Kelvin and Rossby waves are consistent with the delayed oscillator theory (Suarez and Schopf 1988; Battisti and Hirst 1989) that these waves morph into one another by reflection at the

eastern and western boundaries in the Indian Ocean (e.g., Rao et al. 2002; Yamagata et al. 2004; Rao and Behera 2005; Iskandar et al. 2014).

It should be noted that Indonesian precipitation as a trigger of IOD may not be independent of the mechanisms proposed in the previous studies, such as anomalous Hadley and Walker circulations (Annamalai et al. 2003; Fischer et al. 2005). In the context of the large-scale tropical atmospheric circulation, they are dynamically linked with each other. Nevertheless, each of them represents one aspect of the tropical atmosphere and each has its own features. The drivers of Indonesian rainfall anomalies themselves are clearly beyond the scope of this study and not explored here. It is likely, as suggested by Hendon (2003), that there is a positive feedback between IndoP and IOD (also see Fig. 9a, b). Further analysis is needed to establish a more robust understanding of the interactions between IndoP, IOD and ENSO.

Additionally, this study is based solely on the analysis of the no-ENSO run. How ENSO modulates IOD will be a logical extension of this work. Therefore, the next phase of our analysis will focus on the strength of IOD with and without ENSO and how the ENSO perturbations of IndoP may affect IOD and at what timescales and in what season these perturbations may occur. The process understanding presented here with no-ENSO and the impact of ENSO on the intrinsic character of IOD detailed are expected to complete the picture of IOD as it occurs in nature with the totality of interactions between IOD, ENSO and monsoon. As suggested by Behera et al. (2006), ENSO can modulate the intrinsic IOD variability through the Walker circulation. The process likely also involves the ENSO-induced change in IndoP because it is closely related to the convection associated with the rising branch of the Walker circulation. Of course, it is more than likely that there are other passive and active players but those cannot be separated unless the IOD–ENSO–monsoon interactions are fully understood. Through a comparison of the results presented in this paper and further analysis of the ENSO run, the contribution of ENSO in modulating IOD variability will be assessed in a subsequent study.

Acknowledgments The authors would like to thank two anonymous reviewers and the editor for their insightful and constructive comments and suggestions. Partial support from the National Monsoon Mission is gratefully acknowledged.

References

- Ajayamohan RS, Rao SA, Luo J-J, Yamagata T (2009) Influence of Indian Ocean dipole on boreal summer intraseasonal oscillations in a coupled general circulation model. *J Geophys Res: Atmos* 114:D06119. doi:10.1029/2008JD011096
- Aldrian E, Susanto RD (2003) Identification of three dominant rainfall regions within Indonesia and their relationship to sea surface temperature. *Int J Climatol* 23:1435–1452. doi:10.1002/joc.950
- Annamalai H, Murtugudde R, Potemra J, Xie SP, Liu P, Wang B (2003) Coupled dynamics over the Indian Ocean: spring initiation of the zonal mode. *Deep-Sea Res II* 50:2305–2330. doi:10.1016/S0967-0645(03)00058-4
- Battisti DS, Hirst AC (1989) Interannual variability in a tropical atmosphere–ocean model: influence of the basic state, ocean geometry and nonlinearity. *J Atmos Sci* 46:1687–1712
- Behera SK, Luo J-J, Masson S, Rao SA, Sakuma H, Tamagata T (2006) A CGCM study on the interaction between IOD and ENSO. *J Clim* 19:1688–1705
- Behringer DW, Xue Y (2004) Evaluation of the global ocean data assimilation system at NCEP: the Pacific Ocean. In: Eighth symposium on integrated observing and assimilation systems for atmosphere, oceans, and land surface, Seattle, WA, American Meteor Society. http://ams.confex.com/ams/84Annual/techprogram/paper_70720.htm
- Carton JA, Chepurin G, Cao X, Giese BS (2000) A simple ocean data assimilation analysis of the global upper ocean 1950–95. Part I: Methodology. *J Phys Oceanogr* 30:294–309
- Feng M, Meyers G (2003) Interannual variability in the tropical Indian Ocean: a two-year time-scale of Indian Ocean dipole. *Deep-Sea Res* 50:2263–2284
- Feng M, Meyers G, Wijffels S (2001) Interannual upper ocean variability in the tropical Indian Ocean. *Geophys Res Lett* 28:4151–4154
- Feng J, Hu D, Yu L (2014) How does the Indian Ocean subtropical dipole trigger the tropical Indian Ocean dipole via the Mascarene high? *Acta Oceanol Sin* 33:64–76. doi:10.1007/s13131-014-0425-6
- Fischer AS, Terray P, Guilyardi E, Gualdi S, Delecluse P (2005) Two independent triggers for the Indian Ocean dipole/zonal mode in a coupled GCM. *J Clim* 18:3428–3449. doi:10.1175/JCLI3478.1
- Francis PA, Gadgil S, Vinayachandran PN (2007) Triggering of the positive Indian Ocean dipole events by severe cyclones over the Bay of Bengal. *Tellus* 59A:461–475. doi:10.1111/j.1600-0870.2007.00254.x
- Gadgil S, Vinayachandran PN, Francis PA, Gadgil S (2004) Extremes of the Indian summer monsoon rainfall, ENSO and equatorial Indian Ocean oscillation. *Geophys Res Lett*. doi:10.1029/2004GL019733
- Gill AE (1980) Some simple solution for heat-induced tropical circulation. *Quart J Roy Meteor Soc* 106:447–462
- Gnanaseelan C, Vaid BH, Polito PS (2008) Impact of biannual Rossby waves on the Indian Ocean dipole. *Geosci Remote Sensing Lett* 5:427–429
- Hendon HH (2003) Indonesian rainfall variability: impact of ENSO and local air–sea interaction. *J Clim* 16:1775–1790
- Hong C-C, Lu M-M, Kanamitsu M (2008) Temporal and spatial characteristics of positive and negative Indian Ocean dipole with and without ENSO. *J Geophys Res* 113:D08107. doi:10.1029/2007JD009151
- Huang B, Kinter JL III (2002) Interannual variability in the tropical Indian Ocean. *J Geophys Res* 107:3199. doi:10.1029/2001JC001278
- Iskandar I, Mardiansyah W, Setiabudidaya D, Poerwono P, Kurniawati N, Saymsuddin F, Nagura M (2014) Equatorial oceanic waves and the evolution of 2007 positive Indian Ocean Dipole. *Terr Atmos Ocean Sci* 25:847–856. doi:10.3319/TAO.2014.08.25.01(Oc)
- Izumo T, Montegut CB, Luo J-J, Behera SK, Masson S, Yamagata T (2008) The role of the western Arabian Sea upwelling in Indian monsoon rainfall variability. *J Clim* 21:5603–5623
- Izumo T, Vialard J, Lengaigne M, Montegut CB, Behera SK, Luo J-J, Cravatte S, Masson S, Yamagata T (2010) Influence of the

- state of the Indian Ocean dipole on the following year's El Niño. *Nature Geosci* 3:168–172. doi:[10.1038/ngeo760](https://doi.org/10.1038/ngeo760)
- Jin F-F (1997) An equatorial ocean recharge paradigm for ENSO. Part: conceptual model. *J Atmos Sci* 54:811–829
- Kanamitsu M, Ebisuzaki W, Woollen J, Yang S-K, Hnilo JJ, Fiorino M, Potter GL (2002) NCEP-DOE AMIP-II reanalysis (R-2). *Bull Amer Meteor Soc* 83:1631–1643
- Keenlyside NS, Latif M (2007) Understanding equatorial Atlantic interannual variability. *J Clim* 20:131–142. doi:[10.1175/JCLI3992.1](https://doi.org/10.1175/JCLI3992.1)
- Kim ST, Yu J-Y, Kumar A, Wang H (2012) Examination of the two types of ENSO in the NCEP CFS model and its extratropical associations. *Mon Wea Rev* 140:1908–1923
- Kumar A, Wang H, Wang W, Xue Y, Hu Z-Z (2013) Does knowing the oceanic PDO phase help predict the atmospheric anomalies in subsequent months? *J Clim* 26:1268–1285
- Lee T, Waliser DE, Li J-LF, Landerer FW, Gierach MM (2013) Evaluation of CMIP3 and CMIP5 wind stress climatology using satellite measurements and atmospheric reanalysis products. *J Clim* 26:5810–5826
- Li T, Wang B, Chang C-P, Zhang Y (2003) A theory for the Indian Ocean dipole–zonal mode. *J Atmos Sci* 60:2119–2135
- Lübbecke JF (2013) Climate science: tropical Atlantic warm events. *Nature Geosci* 6:22–23. doi:[10.1038/ngro1685](https://doi.org/10.1038/ngro1685)
- Luo J-J, Masson S, Behera S, Yamagata T (2007) Experimental forecasts of the Indian Ocean dipole using a coupled OAGCM. *J Clim* 20:2178–2190
- McPhaden MJ, Nagura M (2014) Indian Ocean dipole interpreted in terms of recharge oscillator theory. *Clim Dyn* 42:1569–1586. doi:[10.1007/s00382-013-1765-1](https://doi.org/10.1007/s00382-013-1765-1)
- Moorthi S, Pan H-L, Caplan P (2001) Changes to the 2001 NCEP operational MRF/AVN global analysis/forecast system. NWS technical procedures bulletin no. 484, 14 pp. <http://www.nws.noaa.gov/om/tpb/484.htm>
- Murtugudde R, McCreary JP Jr, Busalacchi AJ (2000) Oceanic processes associated with anomalous events in the Indian Ocean with relevance to 1997–1998. *J Geophys Res* 105:3295–3306
- Nagura M, Sasaki W, Tozuka T, Luo J-J, Behera SK, Yamagata T (2013) Longitudinal biases in the Seychelles Dome simulated by 35 ocean-atmosphere coupled general circulation models. *J Geophys Res: Oceans* 118:831–846
- Pacanowski RC, Griffies SM (1998) MOM 3.0 manual. NOAA/GFDL 668 pp
- Pan H-L, Mahrt L (1987) Interaction between soil hydrology and boundary layer developments. *Bound-Layer Meteor* 38:185–202
- Pokhrel S, Chaudhari HS, Saha SK, Dhakate A, Yadav RK, Salunke K, Mahapatra S, Rao SA (2012) ENSO, IOD, and Indian summer monsoon in NCEP climate forecast system. *Clim Dyn* 39:2143–2165. doi:[10.1007/s00382-012-1349-5](https://doi.org/10.1007/s00382-012-1349-5)
- Rao SA, Behera SK (2005) Subsurface influence on SST in the tropical Indian Ocean: structure and interannual variability. *Dyns Atmos Oceans* 39:103–135
- Rao SA, Behera SK, Masumoto Y, Yamagata T (2002) Interannual subsurface variability in the tropical Indian Ocean with a special emphasis on the Indian Ocean dipole. *Deep-Sea Res II* 49:1549–1572. doi:[10.1016/S0967-0645\(01\)00158-8](https://doi.org/10.1016/S0967-0645(01)00158-8)
- Saha S et al (2006) The NCEP climate forecast system. *J Clim* 19:3483–3517
- Saji NH, Yamagata T (2003) Structure of SST and surface wind variability during Indian Ocean dipole mode events: COADS observations. *J Clim* 16:2735–2751
- Saji NH, Goswami BN, Vinayachandran PN, Yamagata T (1999) A dipole mode in the tropical Indian Ocean. *Nature* 401:360–363
- Sayantani O, Gnanaseelan C (2014) Tropical Indian Ocean subsurface temperature variability and the forcing mechanisms. *Clim Dyn*. doi:[10.1007/s00382-014-2379-y](https://doi.org/10.1007/s00382-014-2379-y)
- Shi L, Hendon HH, Alves O (2012) How predictable is the Indian Ocean dipole? *Mon Wea Rev* 140:3867–3884
- Shinoda T, Hendon HH, Alexander MA (2004) Surface and subsurface dipole variability in the Indian Ocean and its relation with ENSO. *Deep-Sea Res I* 51:619–635. doi:[10.1016/j.dsr.2004.01.005](https://doi.org/10.1016/j.dsr.2004.01.005)
- Sooraj KP, Annamalai H, Kumar A, Wang H (2012) A comprehensive assessment of CFS seasonal forecasts over the tropics. *Wea Forecasting* 27:3–27
- Sperber KR, Annamalai H, Kang I-S, Kitoh A, Moise A, Turner A, Wang B, Zhou T (2012) The Asian summer monsoon: an intercomparison of CMIP5 vs. CMIP3 simulations of the late 20th century. *Clim Dyn* 41:2711–2744
- Suarez MJ, Schopf PS (1988) A delayed action oscillator for ENSO. *J Atmos Sci* 45:3283–3287
- Sun S, Lan J, Fang Y, Tana Gao X (2015) A triggering mechanism for the Indian Ocean dipoles independent of ENSO. *J Clim* 28:5063–5076
- Wajsovicz RC (2007) Seasonal-to-interannual forecasting of tropical Indian Ocean sea surface temperature anomalies: potential predictability and barriers. *J Clim* 20:3320–3343. doi:[10.1175/JCLI4162.1](https://doi.org/10.1175/JCLI4162.1)
- Wang H, Kumar A (2015) Assessing the impact of ENSO on drought in the U.S. Southwest with the NCEP climate model simulations. *J Hydrol* 526:30–41. doi:[10.1016/j.jhydrol.2014.12.012](https://doi.org/10.1016/j.jhydrol.2014.12.012)
- Wang X, Wang C (2014) Different impacts of various El Niño events on the Indian Ocean dipole. *Clim Dyn* 42:991–1005. doi:[10.1007/s00382-013-1711-2](https://doi.org/10.1007/s00382-013-1711-2)
- Wang B, Wu R, Li T (2003) Atmosphere–warm ocean interaction and its impacts on Asian–Australian monsoon variation. *J Clim* 16:1195–1211
- Wang H, Kumar A, Wang W, Xue Y (2012a) Seasonality of the Pacific decadal oscillation. *J Clim* 25:25–38
- Wang H, Kumar A, Wang W, Xue Y (2012b) Influence of ENSO on Pacific decadal variability: an analysis based on the NCEP climate forecast system. *J Clim* 25:6136–6151
- Wang H, Kumar A, Wang W (2013) Characteristics of subsurface ocean response to ENSO assessed from simulations with the NCEP climate forecast system. *J Clim* 26:8065–8083
- Weare BC, Nasstrom JS (1982) Examples of extended empirical orthogonal function analysis. *Mon Wea Rev* 110:481–485
- Webster PJ, Hoyos CD (2010) Beyond the spring barrier? *Nature Geosci* 3:152–153
- Wilson EA, Gordon AL, Kim D (2013) Observations of the Madden Julian oscillation during Indian Ocean dipole events. *J Geophys Res: Atmos* 118:2588–2599. doi:[10.1002/jgrd.50241](https://doi.org/10.1002/jgrd.50241)
- Wu R, Kirtman BP (2004) Understanding the impacts of the Indian Ocean on ENSO variability in a coupled GCM. *J Clim* 17:4019–4031
- Xie P, Arkin PA (1997) Global precipitation: a 17-year monthly analysis based on gauge observations, satellite estimates, and numerical model outputs. *Bull Amer Meteor Soc* 78:2539–2558
- Yamagata T, Behera SK, Luo J-J, Masson S, Jury M, Rao SA (2004) Coupled ocean–atmosphere variability in the tropical Indian Ocean. *Geophys Monogr* 147:189–212
- Yu J-Y, Lau KM (2005) Contrasting Indian Ocean SST variability with and without ENSO influence: a coupled atmosphere–ocean GCM study. *Meteorol Atmos Phys* 90:179–191. doi:[10.1007/s00703-004-0094-7](https://doi.org/10.1007/s00703-004-0094-7)
- Yuan J, Cao J (2013) North Indian Ocean tropical cyclone activities influenced by the Indian Ocean dipole mode. *Sci China Earth Sci* 56:855–865. doi:[10.1007/s11430-012-4559-0](https://doi.org/10.1007/s11430-012-4559-0)
- Zhang Q, Yang S (2007) Seasonal phase-locking of peak events in the eastern Indian Ocean. *Adv Atmos Sci* 24:781–798
- Zhao Y, Nigam S (2015) The Indian Ocean dipole: a monopole in SST. *J Clim* 28:3–19. doi:[10.1175/JCLI-D-14-00047.1](https://doi.org/10.1175/JCLI-D-14-00047.1)